Copyright WILEY-VCH Verlag GmbH & Co. KGaA, 69469 Weinheim, Germany, 2018.

Supporting Information

Intelligent Metamaterials Based on Nonlinearity for Magnetic Resonance Imaging

Xiaoguang Zhao, Guangwu Duan, Ke Wu, Stephan W. Anderson, and Xin Zhang**

Experimental Section

Fabrication and dimensions of nonlinear metamaterial: The NLMM consists of a linear metamaterial array and a nonlinear varactor-loaded split ring resonator (VLSRR). The unit cell of the linear metamaterial array was composed of copper wire wound around a 3D-printed scaffold. The radius of the wire was 0.28 mm, the radius of the helix was 15 mm, the pitch of the helix was 1.28 mm, and the number of turns was 6.25. In the case of the VLSRR, the radius of the ring was 60 mm and contained a slit which was soldered with a varactor (SMV2020, Skyworks). Details of the NLMM design can be found in Section 2 of the Supporting Information.

Characterization of metamaterial resonance frequency: We employed a network analyzer (E5071C, Keysight Inc) with an inductive loop to excite the magnetic resonance of the VLSRR and the NLMMs and measure the reflection spectrum. In the reflection spectrum, the dip corresponds to the resonance mode of the VLSRR and NLMMs. The incident power was swept from -30 dBm to 0 dBm with a step of 2 dBm. Details of the NLMM characterization can be found in Section 3 of the Supporting Information.

MRI validation: We validated the performance of the NLMMs in improving the signal-to-noise ratio (SNR) of imaging using a 3T MRI system (Philips Healthcare). We placed the NLMMs in the bore of the MRI system and used the body coil for both RF transmission and

reception. A phantom composed of mineral oil was employed for the MRI imaging experiments. Gradient echo imaging was employed with echo time (TE) and repetition time (TR) of 4.6 ms and 100 ms, respectively. The matrix size was 256 × 256 mm, the in-plane resolution was 1 × 1 mm, and the slice thickness was 8 mm. A flip angle of 90° was employed in both control (without NLMM) and NLMM imaging experiments. For comparison, we assessed the performance of a linear MM, which refers to a helical resonator array without the combined VLSRR, by decreasing the excitation energy to avoid overtipping.

For the biological sample validation using an onion and sweet melon, we employed a turbo spin echo (TSE) pulse sequence. In the image acquisition, the echo time (TE) was 80 ms and repetition time (TR) was 3000 ms. The images were captured using the body coil both with and without the NLMMs. Images of the onion were also captured using the LMMs. The matrix size was 208 × 165 and 352 × 345 for the onion and sweet melon, respectively, with pixel size of 0.5 mm and slice thickness of 4 mm. Details of the MRI validation can be found in Section 5 below.

Numerical simulation: The simulation of the NLMM was performed using the finite difference time domain method with CST Microwave Studio software. In the simulation model, the dimensions of the metamaterial were the same as the fabricated sample described above. The scaffold of the metamaterial unit cell was modeled as a dielectric material with permittivity of 2 and a loss tangent of 0.03, the copper wire was considered to be a metal with conductivity of 5.96×10^7 S/m, and the varactor in the VLSRR was modeled as a lump port with capacitance of 3.2 pF. Since it is not feasible to model the field-dependent capacitance of the varactor, we modified the capacitance to fit the response for the high power excitation condition.

SI1. Modeling the nonlinear response

The coupled mode theory is widely employed to describe the response of electromagnetic systems. In the case of a linear resonator, the relationship between the mode amplitude and the excitation signal is expressed by:

$$\frac{da_1}{dt} = \left[j\omega_{o1} - \frac{1}{\tau_{e1}} - \frac{1}{\tau_{01}} \right] a_1 + \sqrt{\frac{2}{\tau_{e1}}} s_+ \tag{5}$$

where a_1 is the mode amplitude of the resonator, ω_{o1} is the resonance frequency, $1/\tau_{e1}$ and $1/\tau_{01}$ are the decay rates due to radiation and intrinsic losses, respectively, and s_+ is the excitation signal. The collective resonance mode of a metamaterial composed of multiple unit cells may be considered as a single resonator. When a nonlinear resonance component is proximate to the linear resonator, the resonance strength of the linear resonance may be controlled by the nonlinear resonator. One form of a nonlinear resonator is a varactor-loaded split resonator (VLSRR), as shown in Fig. 1b in the main text, in which the resonance frequency is related to the oscillation strength in the resonator. For a single VLSRR, its mode amplitude is related to the excitation signal by:

$$\frac{da_2}{dt} = \left[j\omega_2 - \frac{1}{\tau_{e2}} - \frac{1}{\tau_{02}} \right] a_2 + \sqrt{\frac{2}{\tau_{e2}}} s_+ \tag{6}$$

in which ω_2 is the resonance frequency of the VLSRR, which is dependent upon the oscillation strength of the resonator ($|a_2|$) as described below, and $1/\tau_{e2}$ and $1/\tau_{02}$ are decay rates due to radiation and intrinsic losses, respectively. The resonance frequency may be expressed as $\omega_2 = 1/\sqrt{(LC)}$, in which L is predominately attributed to the inductance of the loop and C corresponds to the capacitance of the varactor. The capacitance of the varactor is related to the voltage across it by (*30*):

$$C(V_D) = C_0 \left(1 - \frac{V_D}{V_P} \right)^{-M} \approx C_0 + V_D \frac{C_0 M}{V_P} \tag{7}$$

where C_0 is the initial capacitance, V_D is the voltage across the varactor, M is a fitting exponent, and V_P is the intrinsic potential of the varactor obtained from the data sheet. The resonance frequency of the VLSRR is expressed as:

$$\omega_2 = \frac{1}{\sqrt{LC}} \approx \frac{1}{\sqrt{LC_0}} - \frac{1}{2\sqrt{LC_0}} \frac{\Delta C}{C_0} \tag{8}$$

By inserting (3) into (4), we obtain:

$$\omega_2 = \frac{1}{\sqrt{LC_0}} - \frac{1}{2\sqrt{LC_0}} \frac{V_D M}{V_P} \tag{9}$$

As the voltage accumulating across the varactor increases, the resonance frequency of the nonlinear SRRs increases, leading to a blueshift of the resonance frequency. By inserting Eq. (5) into Eq. (2), the following is obtained:

$$\frac{da_2}{dt} = \left[j(\omega_{o2} - \lambda_0 |a_2|) - \frac{1}{\tau_{e2}} - \frac{1}{\tau_{02}} \right] a_2 + \sqrt{\frac{2}{\tau_{e2}}} s_+ \tag{10}$$

in which $\lambda_0 = \omega_0 M/(2V_p)$ is a constant related to the properties of the varactor. Assuming the excitation is a harmonic function with frequency ω (i.e. $s_+ = |s_+|e^{j\omega t}$), the amplitude of the VLSRR may be calculated by numerically solving the nonlinear equation:

$$j\omega a_2 = \left[j\left(\omega_{o2} - \lambda_0 |a_2|\right) - \frac{1}{\tau_{e2}} - \frac{1}{\tau_{02}} \right] a_2 + \sqrt{\frac{2}{\tau_{e2}}} |s_+| \tag{11}$$

The solutions of Eq. (7) as a function of driving frequency (ω) are shown in Fig. S1a. When the excitation energy ($|s_+|$) is low, a strong resonance exists in the coil, similar to the linear response, since the effect of the nonlinear term is negligible. When the excitation strength ($|s_+|$) is high, there are three roots of $|a_2|$ and the curve assumes an oblique orientation. The curve may be divided into three distinct branches, the lower, middle and higher branches. The middle branch is unstable and the oscillation tends to jump to the other two branches. In the operation of the VLSRR, the oscillation response follows the lower branch and, as the

frequency increases, the response jumps to the higher branch at the frequency corresponding to the intersection of the lower and middle branches. Ultimately, the oscillation of the VLSRR is a bi-stable response, which agrees well with the experimental results. In the experimental analyses, we measured the reflection coefficient via a loop antenna. The reflection coefficient may be calculated by (*35*):

$$r = -1 + \sqrt{\frac{2}{\tau_{e2}}}\frac{a_2}{s_+} \tag{12}$$

The calculated reflection response (Fig. S1b) is in agreement with the experimental results, as will be shown below.

When the two resonators, i.e. the linear metamaterial (LMM) resonator and the VLSRR, are coupled to form a NLMM, the overall response of the NLMMs is modulated by the incident energy intensity. The response of the NLMM within the framework of the coupled-mode theory (CMT) is given by considering the coupling factor between two resonators (*35*):

$$\frac{da_1}{dt} = \left[j\omega_{o1} - \frac{1}{\tau_{e1}} - \frac{1}{\tau_{01}} \right] a_1 + jka_2 + \sqrt{\frac{2}{\tau_{e1}}} s_+ \tag{13}$$

$$\frac{da_2}{dt} = \left[j\left(\omega_{o1} + \Delta\omega - \lambda_0 |a_2|\right) - \frac{1}{\tau_{e2}} - \frac{1}{\tau_{02}} \right] a_2 + jka_1 + \sqrt{\frac{2}{\tau_{e2}}} s_+ \tag{14}$$

By converting the time domain differential equation to the frequency domain, we obtain:

$$\left[j\left(\omega - \omega_{o1}\right) + \frac{1}{\tau_{e1}} + \frac{1}{\tau_{01}} \right] a_1 = jka_2 + \sqrt{\frac{2}{\tau_{e1}}} |s_+| \tag{15}$$

$$\left[j\left(\omega - \omega_{o1} - \Delta\omega + \lambda_0 |a_2|\right) + \frac{1}{\tau_{e2}} + \frac{1}{\tau_{02}} \right] a_2 = jka_1 + \sqrt{\frac{2}{\tau_{e2}}} |s_+| \tag{16}$$

By substituting the solution of a_1 from Eq. (11) to Eq. (12), we obtain:

$$\left[j\left(\omega-\omega_{o1}\right)+\frac{1}{\tau_{e1}}+\frac{1}{\tau_{01}}\right]\left[j\left(\omega-\omega_{o1}-\Delta\omega+\lambda_0\left|a_2\right|\right)+\frac{1}{\tau_{e2}}+\frac{1}{\tau_{02}}\right]a_2 = -k^2 a_2+jk\sqrt{\frac{2}{\tau_{e1}}}\left|s_+\right|+jk\sqrt{\frac{2}{\tau_{e1}}}\left|s_+\right|+\left[j\left(\omega-\omega_{o1}\right)+\frac{1}{\tau_{e1}}+\frac{1}{\tau_{01}}\right]\sqrt{\frac{2}{\tau_{e2}}}\left|s_+\right| \tag{17}$$

Finally, the following is obtained:

$$\left\{\left[j\left(\omega-\omega_{o1}\right)+\frac{1}{\tau_{e1}}+\frac{1}{\tau_{01}}\right]\left[j\left(\omega-\omega_{o1}-\Delta\omega+\lambda_0\left|a_2\right|\right)+\frac{1}{\tau_{e2}}+\frac{1}{\tau_{02}}\right]+k^2\right\}a_2 = jk\sqrt{\frac{2}{\tau_{e1}}}\left|s_+\right|+\left[j\left(\omega-\omega_{o1}\right)+\frac{1}{\tau_{e1}}+\frac{1}{\tau_{01}}\right]\sqrt{\frac{2}{\tau_{e2}}}\left|s_+\right| \tag{18}$$

By solving Eq. (14), the mode amplitude of the VLSRR (a_2) as a function of incident power is derived. The mode amplitude of the linear metamaterial resonator (a_1) is given by:

$$a_1=\frac{jka_2+\sqrt{\frac{2}{\tau_{e1}}}\left|s_+\right|}{j\left(\omega-\omega_{o1}\right)+\frac{1}{\tau_{e1}}+\frac{1}{\tau_{01}}} \tag{19}$$

The reflection from the NLMMs when probed by a coupling loop is calculated by:

$$r=-1+\frac{\sqrt{\frac{2}{\tau_{e1}}}a_1+\sqrt{\frac{2}{\tau_{e2}}}a_2}{2\left|s_+\right|} \tag{20}$$

The theoretical results are in close agreement with the measured results using the following parameters: $\omega_{o1} = 2\pi\times127\times10^6$ (rad/s), $\tau_{o1} = 650/\omega_{o1}$, $\tau_{e1} = 3300/\omega_{o1}$, $\tau_{o2} = 120/\omega_{o1}$, $\tau_{e2} = 132/\omega_{o1}$, $k = 0.031\omega_{o1}$, $\Delta\omega = 0.0122\omega_{o1}$, and $\lambda_0 = 0.1648\omega_{o1}$.

We employed the ODE15 function in MATLAB to solve the nonlinear differential equations (Eqs. (9) and (10)) numerically to yield the time domain results. We assumed that the excitation is a sine wave with frequency of 127 MHz, which is the resonance frequency of the coupled NLMM. We calculated the time domain mode amplitude of the LMM (a_1) for low and high amplitude states of excitation $|s_+|$, as shown in Fig. S2. For the low energy excitation

state, the NLMM exhibits strong resonance and the response time of the resonator is approximately 0.2 μs. For the high energy excitation state, the magnitude of the mode amplitude is ~ 1/16 of the low energy excitation state, and is highly distorted due to the nonlinear response. The calculated time domain result further supports the conclusion that the NLMM remains silent during the high energy excitation state and resonates during the low energy excitation state.

SI2. Fabrication and dimensions of nonlinear metamaterial

The NLMM consists of a linear metamaterial array and a nonlinear varactor-loaded split ring resonator (VLSRR). The unit cell of the linear metamaterial array was composed of copper wire wound around a 3D-printed scaffold. The radius of the wire (r_w) was 0.28 mm, the radius of the helix (r_a) was 15 mm, the pitch of the helix (p) was 1.28 mm, and the number of turns (N) was 6.25. In the case of the VLSRR, the radius of the ring was 60 mm and contained a slit which was soldered with a varactor (SMV2020, Skyworks). The schematic of the NLMMs is shown in Fig. S3. The nominal capacitance of the varactor (C_0) was 3.2 pF at the initial state. For the varactor, V_P was 4.4 V and M was 1.45, from the datasheet. The vertical distance between the linear metamaterial resonator and the VLSRR was ~ 30 mm, thereby assuring moderate coupling between these components. The unit cell number and the distance between adjacent unit cells in the LMM array were designed such that the resonance frequency of the NLMM matched the operating frequency of the MRI, which is 127 MHz for the 3T MRI system employed herein. We employed two designs of the NLMMs, one of which featured two unit cells while the other was composed of a 4 x 4 unit cell array in the linear metamaterial. For the two unit cell design, the separation distance (d) between the unit cells was ~1.8 mm and in the case the 4 x 4 unit cell design, d was ~3.0 mm.

SI3. Characterization of metamaterial resonance frequency

In order to characterize the resonance frequency of the NLMMs, we employed a network analyzer (E5071C, Keysight Inc) with an inductive loop to excite the magnetic resonance of the VLSRR and the NLMMs and measure the reflection spectrum, as shown in Fig. S4. In the reflection spectrum, the dip corresponds to the resonance mode of the VLSRR and NLMMs. The incident power was swept from -30 dBm to 0 dBm with a step of 2 dBm.

In the case of the VLSRR, the resonance frequency was ~ 132.5 MHz when the incident power was low. As the incident power increased, the resonance shifted to lower frequencies and a sudden jump in the frequency eventually emerged, demonstrating a bi-stable nonlinear response. A similar response may be obtained using the CMT model, with the agreement between the experimental results and theoretical analysis serving to validate the CMT model.

In the case of the coupled NLMMs consisting of two unit cells, there are two resonance modes in the reflection coefficient. The first mode is the collaborative resonance mode, in which the resonance in the linear MMs and VLSRR are in phase. For low incident power, the NLMM resonance occurs at 127 MHz while with high incident power, the resonance at 127 MHz diminishes. These results are discussed in detail in the main text.

In the response of the coupled NLMMs consisting of 4 x 4 unit cells, as shown in Fig. S4f, additional parasitic resonance modes appeared with the collaborative resonance mode located at ~ 127 MHz for low incident power. For high incident power, the resonance of the NMM diminished, similar to the two unit cell case.

SI4. Calculation of the magnetic field and SNR enhancement

The magnetic field enhancement factor in the metamaterial can be calculated based on Faraday's law and the Biot and Savart law. If there is an incident magnetic field $\mathbf{B_0}(t)$ [$\mathbf{B_0}(t) = \mathbf{B_0}\exp(-j\omega t)$] with polarization along the axis of the unit cell helices, the voltage, or electromotive force (emf), induced in a helix is:

$$V = N\frac{d\Phi}{dt} = NA\frac{d\mathbf{B}_o(t)}{dt} \tag{21}$$

where $A = \pi r_c^2$ is the area surrounded by the coil, r_c is the radius of the helix, and N is the number of turns of the helix. The impedance of the helix is modeled by (*21*):

$$Z = R + j\omega L + \frac{1}{j\omega C} \tag{22}$$

in which R is the overall resistance of the helix, including the ohmic and dielectric losses, L and C are the equivalent inductance and capacitance of the helix, taking the self-reactance and mutual reactance into account. The induced current in the helix is calculated by:

$$I = \frac{V}{Z} \tag{23}$$

The induced magnetic field at a specific position ($\mathbf{r_p}$) can be calculated via the line integral along the helix curve:

$$\mathbf{B}\left(\boldsymbol{r}_p\right) = \frac{\mu_0}{4\pi}\oint I_d(\boldsymbol{r})\frac{d\boldsymbol{s}\times\left(\boldsymbol{r}_p-\boldsymbol{r}\right)}{\left|\boldsymbol{r}_p-\boldsymbol{r}\right|^3} \tag{24}$$

in which $\boldsymbol{r_p}$ and $\boldsymbol{r}$ are vectors pointing to the $d\boldsymbol{s}$ on the coil and the observing point from the origin, respectively, d$\boldsymbol{s}$ is the vector representing an infinitely small section on the helix, and $I(\boldsymbol{r})$ is the current at this point, which as shown in Fig. S5. The overall magnetic field at $\boldsymbol{r_p}$ can be evaluated by combining the contribution from each unit cell helix in the NLMM, the nonlinear coil, and the incident field. Therefore, the magnetic field enhancement ratio is:

$$R_B\left(\boldsymbol{r}_p\right) = \frac{\left|B_z\left(\boldsymbol{r}_p\right)+B_0\right|}{\left|B_0\right|} \tag{25}$$

Notably, R_B is a function of frequency and is at a maximum at the resonance frequency of the NLMMs.

The SNR is a function of the operating frequency (ω_0), the receive magnetic field (B_1^-) and the overall resistance of the sample and coil (R_s and R_c, respectively) by (*38*):

$$SNR \propto \frac{\omega_0^2 B_1^-}{\sqrt{R_s + R_c}} \tag{26}$$

in which B_1^- refers to the magnetic strength induced by an assumed unit current in the readout coil. This equation is valid for homogeneous excitation during the transmission phase. The R_s term is the equivalent resistance of the sample (phantom or human body) to the coil, which may be evaluated by the power loss in the sample for the unit current in the readout coil.

We performed a full wave simulation of the MRI birdcage body coil to calculate that the magnetic field induced by a unit (1 A) current is ~ $3.17\mu_0$ T and is uniformly distributed in the bore of the MRI in the absence of a metamaterial. The resistivity (ρ) of the phantom during this simulation was ~ 10 Ω·m. The phantom is a cylinder with radius (r_s) of 5 cm and height (h) of 20 cm. The total power dissipated by the phantom is (*30*):

$$P = \int_0^{r_s} \int_0^h \frac{\pi r^3}{4\rho} B_1^- (r,h)^2 \, \omega^2 dh dr \tag{27}$$

In the absence of the metamaterial, the magnetic field is uniformly distributed and the dissipated power is found to be ~ 0.272 W. Therefore, the resistance of the sample ($R_{s,0}$) is 0.2724 Ω. From the full wave simulation, the resistance of the birdcage body coil was derived, which was approximately 9.9 Ω.

In the presence of the nonlinear metamaterial, gradients in the magnetic field (B_1^-) are induced. We assumed that the magnetic field is uniform in a cross-section of the phantom and only decays along the z-axis. We considered the magnetic field enhancement factor calculated by Eq. (21) in the calculation of total power dissipation, which was found to be 4.305 W. Therefore, the resistance ($R_{s,1}$) of the sample in the presence of the NMMs was 4.305 Ω. The SNR enhancement ratio at an arbitrary location is given by:

$$R_{SNR} = R_B(\boldsymbol{r_p}) \frac{\sqrt{R_{s,0} + R_c}}{\sqrt{R_{s,1} + R_c}} \tag{28}$$

In the presence of a linear metamaterial, the SNR exhibits a steeper gradient in its decline with increasing distance from the metamaterial due to the non-uniform excitation in the transmission phase, and may be described as (*28*):

$$R_{SNR} = \sin\left[\frac{R_B(\boldsymbol{r_p})}{\max\left[R_B(\boldsymbol{r_p})\right]}\frac{\pi}{2}\right] R_B\left(\boldsymbol{r_p}\right)\sqrt{\frac{R_{s,0}+R_c}{R_{s,1}+R_c}} \tag{29}$$

The theoretical results derived in this fashion are in good agreement with experimental results, as shown in Fig. 3d of the main text.

SI5. MRI validation

We validated the performance of the NLMMs in improving the signal-to-noise ratio (SNR) of imaging using a 3T MRI system (Philips Healthcare). We placed the NLMMs in the bore of the MRI system and used the body coil for both RF transmission and reception, as shown in Fig. S6. A phantom composed of mineral oil was employed for the MRI imaging experiments. Gradient echo imaging was employed with echo time (TE) and repetition time (TR) of 4.6 ms and 100 ms, respectively. The matrix size was 256 x 256 mm, the in-plane resolution was 1 x 1 mm, and the slice thickness was 8 mm. A flip angle of 90° was employed in both control (without NLMM) and NLMM imaging experiments. In order to measure the SNR, a magnitude image was captured as the signal, as shown in Fig. S7a, and the noise was calculated as the standard deviation of the image captured when the transmission amplifier remained off (Fig. S7b). The measured SNR was calculated by $SNR = I_{signal}/STD_{noise}$. For comparison, we assessed the performance of a linear MM, which refers to a helical resonator array without the combined VLSRR, by decreasing the excitation energy to avoid overtipping. For the experiment employing the BC alone, the flip angle (FA) of the entire phantom was 90° and a uniform image/SNR are achieved. In the case of the LMM, the energy of the excitation RF field was reduced by a factor of 5 (18°) in order to ensure that the FA along the bottom of phantom, in proximity to the transmission RF-magnifying metamaterial, did not

exceed 90°. Therefore, due to the gradient in the magnetic field enhancement of LMM, the FA in the region near the top of the phantom was significantly less than 90°.

B1+ mapping, using the dual-TR approach (*3*), was also employed to analyze the effect of the metamaterial arrays on RF transmission energy, with the results for both the LMMs and NLMMs shown in Fig. S8. Initially, an excitation flip angle of 60° was used. In the case of the LMMs, due to their multi-fold enhancement of the transmission magnetic field, dark bands are induced, which correspond to an actual flip angle of n × 180° (n being an integer) in the B1 map. The dark bands induced in this fashion are overtip artifacts in the MRI image (Fig. S8a). In order to avoid overtipping, the flip angle was reduced to 18° by reducing the transmission magnetic field strength. As shown in Fig. S8b, the B1 map demonstrates a higher signal in proximity to the LMM, with a dramatic decrease in the upper portion of the phantom. The gradient in the RF excitation decreases the signal strength with increasing distance from the LMM. In the case of the NLMMs, a flip angle of 60° was used and a uniform B1 map was obtained, as shown in Fig. S8c. This supports the conclusion that the NLMMs were not interacting with the RF magnetic field to any significant degree and remained in their ‘off’ state during the transmission phase, as is desired. As a result, more gradual decay of the SNR enhancement was achieved with the NLMM when compared to the LMM.

For the biological sample validation using an onion and sweet melon, we employed a turbo spin echo (TSE) pulse sequence. In the image acquisition, the echo time (TE) was 80 ms and repetition time (TR) was 3000 ms. The images were captured using the body coil both with and without the NLMMs. Images of the onion were also captured using the LMMs. The matrix size was 208 x 165 and 352 x 345 for the onion and sweet melon, respectively, with pixel size of 0.5 mm and slice thickness of 4 mm in both cases.

SI6. MRI image of the sweet melon

We imaged a sweet melon using a TSE pulse sequence; the results are shown in Fig. S9. Similar to both the phantom and onion imaging, the SNR is markedly improved, particularly along the bottom portion of the melon.

SI7. MRI imaging using a 4 × 4 NLMM array

A NLMM consisting of 4 × 4 array of helical resonators coupled to a VLSRR was also employed to boost the SNR of the MRI, with the 4 x 4 LMM counterpart characterized for comparison. As shown in Fig. S10, the 4 × 4 NMM exhibited a peak SNR enhancement ratio of 7.4 and a decay length of 15 cm, while the 4 × 4 LMM had a peak SNR enhancement ratio of 6.2 and decay length of 8 cm. These results demonstrate that the scheme to construct NLMMs using coupled LMMs with a VLSRR serves to enhance the SNR of MRI for varied designs of the LMM.

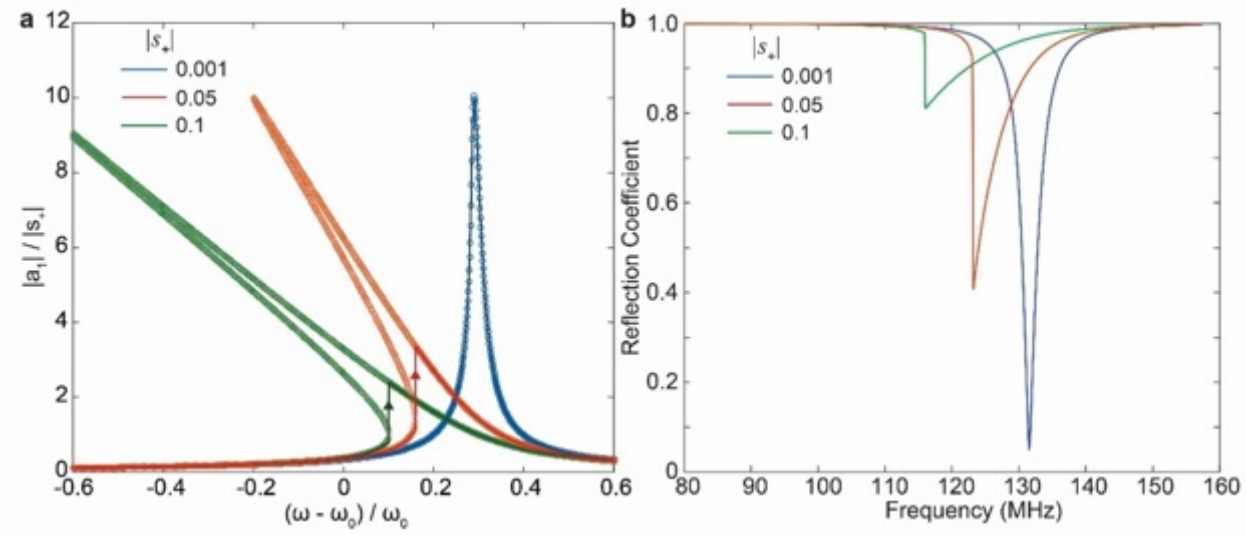

Figure S1. a) The oscillation amplitude of the VLSRR as a function of the driven frequency for different excitation strengths calculated from the lumped nonlinear model. The arrows demonstrate the jump between two stable responses as the frequency increases. b) The calculated reflection spectrum of the VLSRR for varied excitation strength.

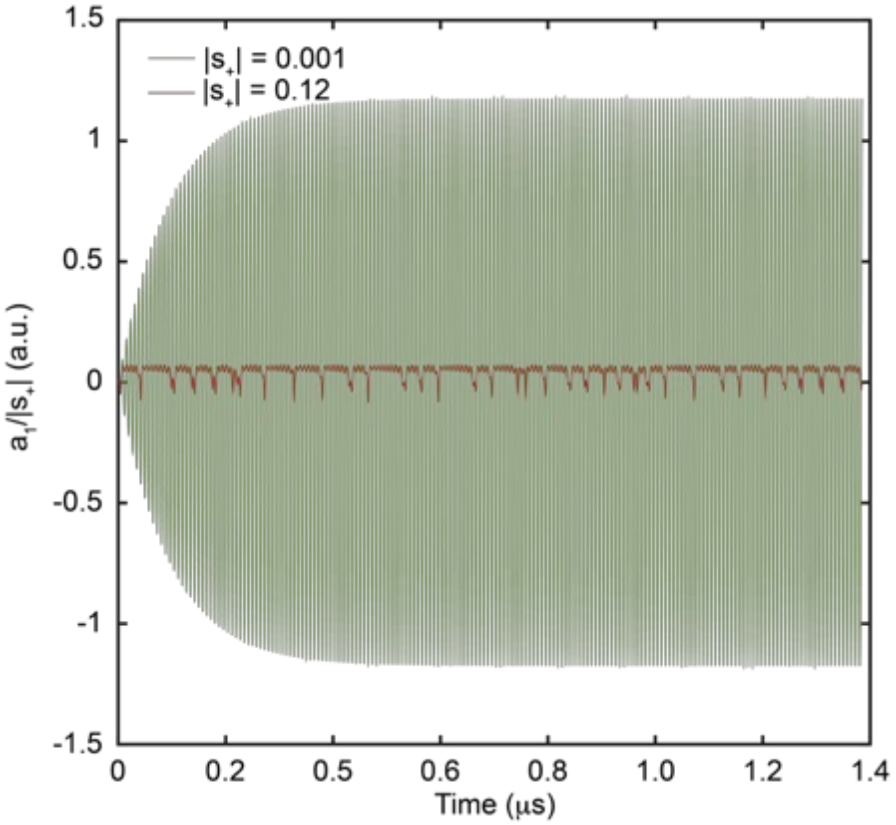

Figure S2. The calculated time domain response of the NLMM for low excitation strength and high excitation strength.

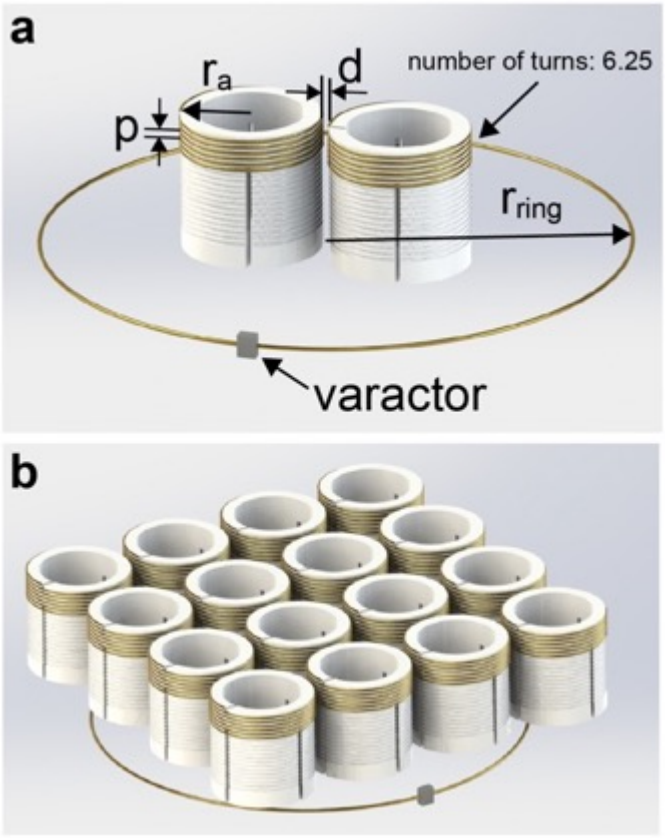

Figure S3. Schematic of the nonlinear metamaterials consisting of 2 × 1 a) and 4 × 4 b) helical resonators.

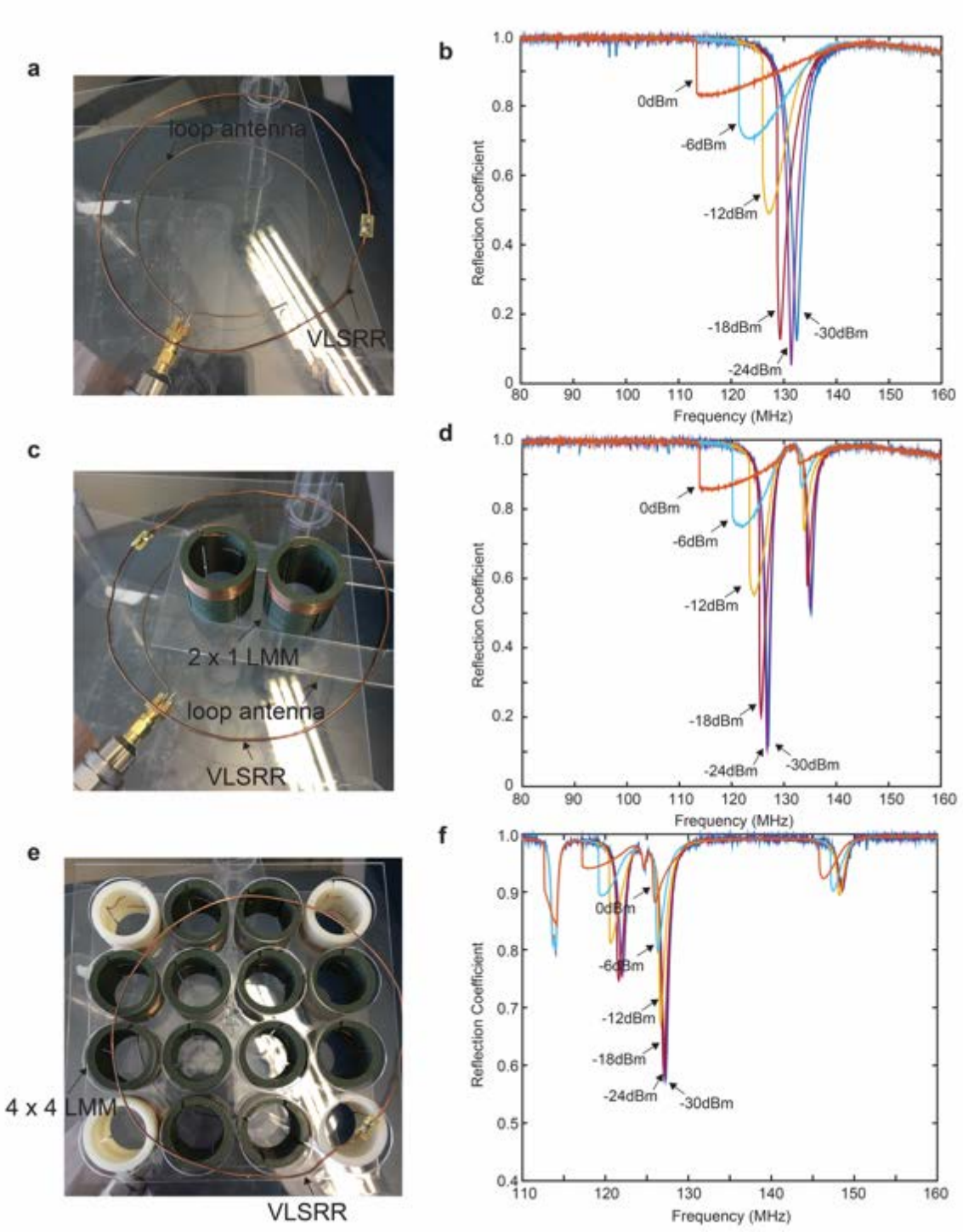

Figure S4. Experimental validation of the nonlinear response. Experimental configurations a), c), and e) for characterization of the VLSRR, 2 × 1 NLMM, and 4 × 4 NLMM, respectively, and corresponding reflection coefficients b), d), and f).

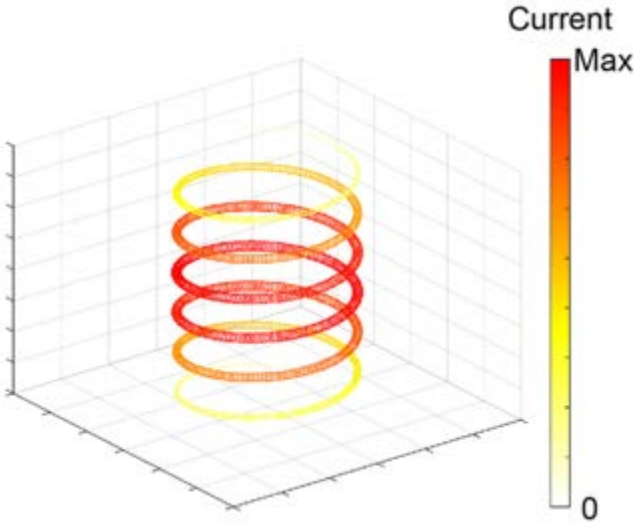

Figure S5. Current distribution along the helix at the resonance state for the calculation of the magnetic field enhancement.

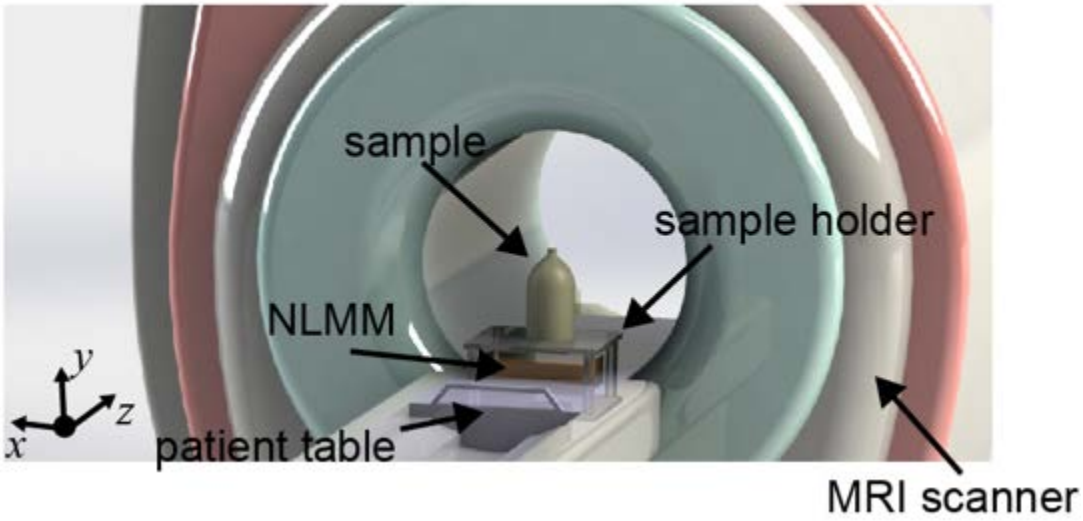

Figure S6. Illustration of the experimental setup to characterize the MRI performance of the nonlinear metamaterial (NLMMs).

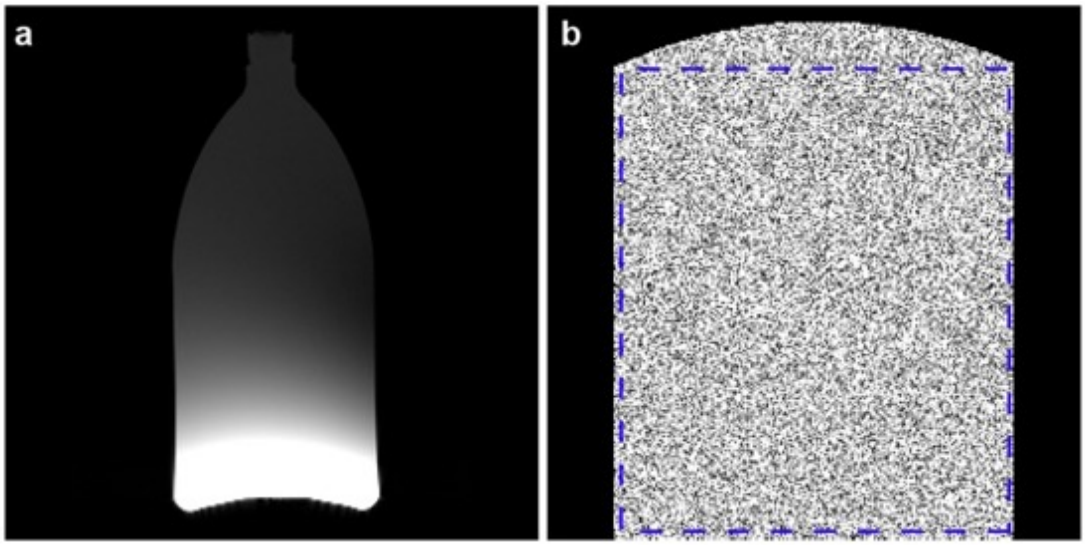

Figure S7. a) MRI image of the phantom in the presence of the NLMM, used to measure the signal. b) Image capture with the transmission amplifier off, the standard deviation of which (blue frame) was employed to derive image noise.

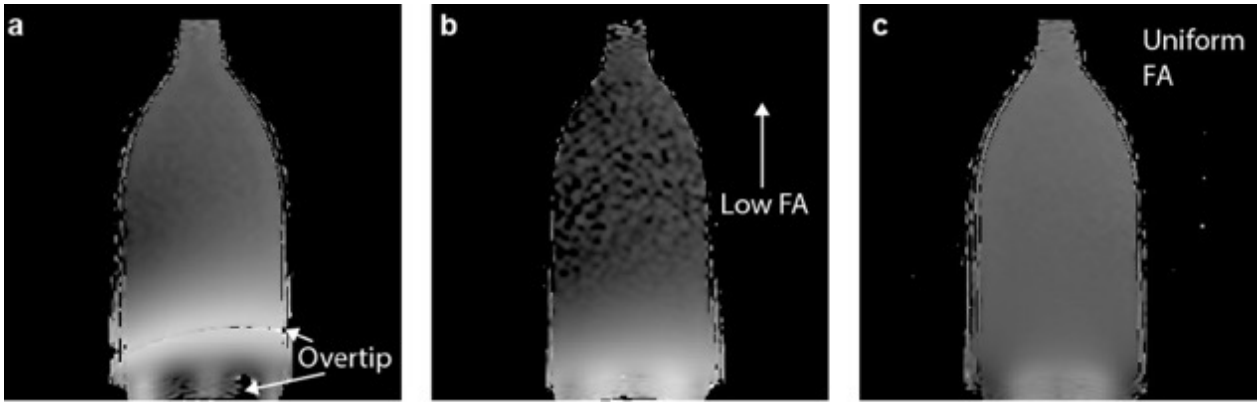

Figure S8. a) and b) are the B1 maps for the linear MMs with preset flip angles of 60° and 18°, respectively. c) B1 map for the NLMMs with flip angle of 60°.

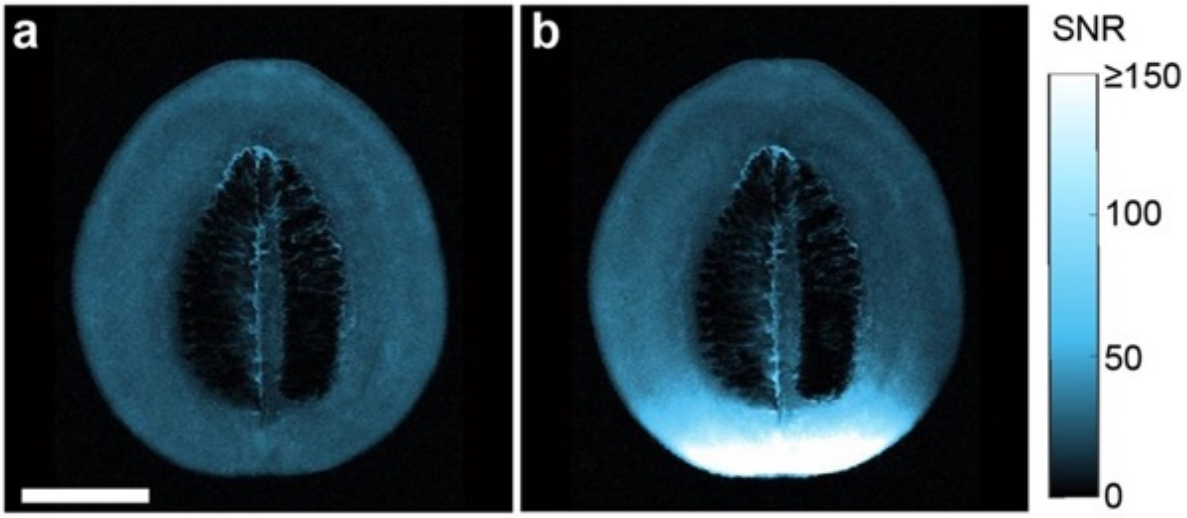

Figure S9. 3T MRI imaging of sweet lemon. Spin echo imaging employed. Images of the sweet melon without a) and with b) the NLMM. Scale bar is 5 cm.

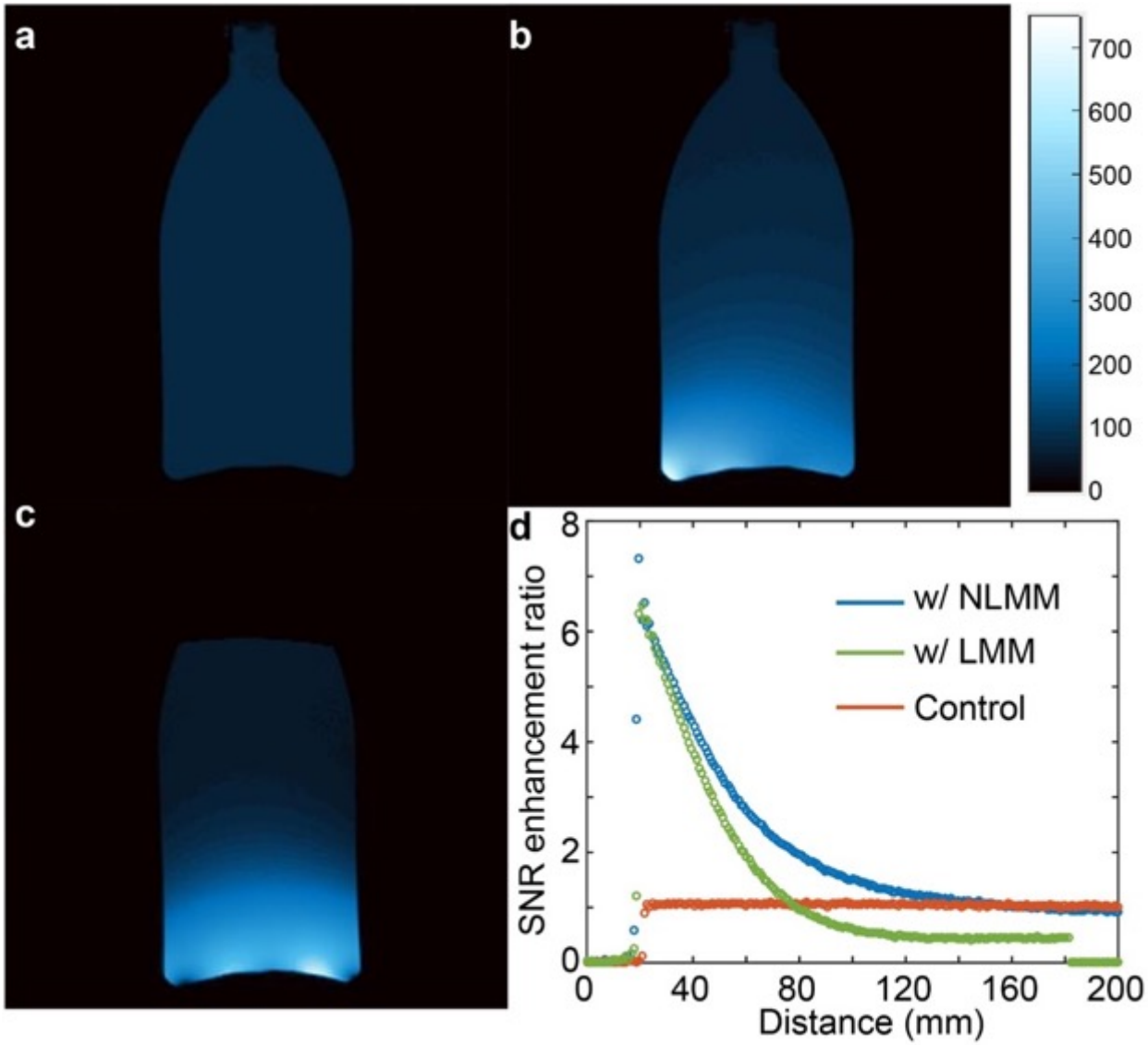

Figure S10. **MRI images of a phantom captured using a clinical 3T MRI**. **a**) Image captured by the body coil in the absence of metamaterials. **b**) Image captured by the body coil with the NLMM consisting of 4 × 4 helical resonators. **c**) Image captured by the body coil with the linear MMs consisting of 4 × 4 helical resonators. **d**) Comparison of the SNR enhancement ratio for the nonlinear and linear MMs.